A new approach to model delamination growth in fatigue using the Virtual Crack Closure Technique without re-meshing

N. V. De Carvalho[a,*], G.E. Mabson[b], R.Krueger[a], L.R. Deobald[b]

[a] *National Institute of Aerospace, resident at: Durability, Damage Tolerance and Reliability Branch, NASA Langley Research Center, Hampton, VA 23681-2199, USA*
[b] *The Boeing Company, Seattle, WA, 98124, USA*

Abstract

A modeling approach is proposed to simulate delamination propagation in fatigue that combines the Virtual Crack Closure Technique (VCCT) with a progressive nodal release strategy. The progressive nodal release alleviates the artificial stress concentrations found when using the VCCT with instantaneous release to model 3D delamination without re-meshing. This enables crack shapes that do not conform to the underlying mesh to be readily simulated. The progressive release is formulated such that no artificial growth or healing occurs as a result of a change in loading conditions. Furthermore, expressions for calculating energy release rates at partially released nodes are proposed and applied to arbitrarily shaped delamination fronts. The shape of the delamination front is considered explicitly in the energy release rate calculations, and is determined by considering the normalized crack positions associated with the partial nodal release. Contrary to previous implementations, the local delamination propagation direction is not assumed to follow mesh lines, but instead is computed as part of the iterative procedure proposed to determine the maximum energy release along the crack front. The results obtained suggest the approach can accurately simulate Mode I, Mixed Mode I/II and Mode II fatigue delamination growth and be used to simulate growth of arbitrarily shaped cracks that do not conform to the underlying mesh.

Keywords: Delamination; Fracture; Fatigue; Finite element analysis; Virtual Crack Closure Technique; Floating Node Method

*Corresponding author: Telephone/Fax: +1 757 864 4505/+1 757 864 8911
Email address: nelson.carvalho@nasa.gov (N. V. De Carvalho)

1. Introduction

Delamination is one of the most common and critical failure modes in composites [1]. Within the Finite Element Method framework, the Virtual Crack Closure Technique (VCCT) [2, 3] and Cohesive Zone (CZ) approaches (e.g. [4, 5]) have become the most commonly used techniques for simulating delamination propagation in composites. Implementations of these techniques, mostly aimed at simulating quasi-static delamination growth, can now be found in several commercial software packages. However, modeling delamination growth, particularly under fatigue loading, remains a challenge and an active area of research. Although approaches requiring enhanced element formulations [6] or alternative numerical frameworks [7] have been proposed recently, most of the research on the simulation of delamination growth in fatigue focuses on the enhancement and maturing of the VCCT and CZ approaches and their application, e.g. [8–10].

The present work proposes a new technique that couples the VCCT with a progressive nodal release strategy to enable the modeling of fatigue crack growth of arbitrarily shaped delaminations without re-meshing. The VCCT is a numerical method used to determine Energy Release Rate (ERR) components. However, modeling crack growth in an automatic fashion, based on the ERRs computed using the VCCT, requires a separate strategy. One such strategy consists of updating the mesh near the crack front such that, at each growth increment, it conforms to the crack shape. This method typically renders very accurate results [11–13]. However, challenges arise when modeling the interaction of multiple in-plane delaminations [12], as well as overlapping through-thickness delaminations. These are non-trivial challenges to re-meshing algorithms that have not yet, to the best of the authors' knowledge, been unequivocally addressed. Alternatively, a second strategy can be found in literature, in which a delamination is propagated without updating the mesh, by fully releasing penalty stiffnesses associated with each element or node, e.g., [14, 15]. However, as a result of this procedure, the shape of the crack front is forced to conform to the underlying mesh, resulting in jagged crack fronts that cause artificial stress concentrations which in turn affect the accuracy of the ERR calculations. For 2D problems, where each crack tip is at a single node, or simple 3D geometries in which crack front and mesh remain aligned as the crack propagates, this procedure may provide sufficiently accurate results, e.g., [14, 15]. However, recognizing this limitation, particularly for cracks that develop with an arbitrary shape,

several methods have been proposed to alleviate the artificial local stress concentrations and their effect on the ERR calculation. These methods typically focus on the use of correction factors applied to the VCCT expressions, e.g., [16–18]. These correction factors can be non-trivial both to implement, in particular if accounting for multiple interacting delaminations, and to verify. Furthermore, they only partially alleviate the effect of the artificial stress concentrations on the ERR calculation and, more importantly, do not remove the artificial stress concentrations.

The present work is based on the methodology proposed in [19]. In [19], an alternative approach was proposed in which intermediate crack positions that do not conform to the mesh are accommodated by allowing the nodes to be released progressively via the use of kinematic constraints that change as the crack grows between node pairs. The approach was implemented via an interface element [19] and applied to the simulation of quasi-static delamination growth in 2D. A similar approach has been implemented in Abaqus/Standard [20] and can be applied to simulate delamination growth in 3D, but is presently limited to quasi-static applications. The use of progressive release alleviates the stress concentrations caused by a potential mismatch between the underlying mesh and the crack front. The present work follows recent efforts from the authors [21] and extends the methodology proposed in [19] to fatigue applications. A new treatment of the progressive release under mixed-mode conditions is formalized which ensures that no artificial crack growth/healing occurs as a result of a change in mode-mixity. In addition, a new procedure to determine ERR that explicitly takes into account the local crack shape and does not assume the local delamination growth direction is proposed and applied to arbitrarily shaped planar cracks.

A summary of the methodology used to determine ERRs is provided in the next section (Section 2). Subsequently, the progressive release procedure and its implementation to model fatigue crack growth are presented in Section 3. Illustrative numerical results are presented in Section 4, including quantitative and qualitative comparison to existing benchmarks, followed a discussion of the results obtained and conclusions in Sections 5 and 6, respectively.

2. Energy release rate calculation

Progressive nodal release is used, in the present study, to represent intermediate crack positions between node pairs. The concept of progressive nodal release, in the context of VCCT, is illustrated in Figure 1 as proposed in [19]. Assume the crack grows past node position i to some intermediate position between node i and $j+2$. In the method proposed in [19], the propagation to an intermediate position between nodes is represented by a kinematic constraint inserted between the top and bottom surface nodes at the nodal position i. This kinematic constraint can be thought of as springs connecting the degrees of freedom of nodes i^+ and i^-. The stiffness of these springs is assigned according to the algorithm detailed in Section 3. The progressive release procedure results in a region across the crack front where nodes may be at an intermediate stage of release, held by kinematic constraints. This region is akin to a process zone obtained in cohesive element formulations. However, contrary to a process zone obtained in cohesive element formulations, this region is always defined by the distance between adjacent node pairs and does not intend to represent a material constitutive response.

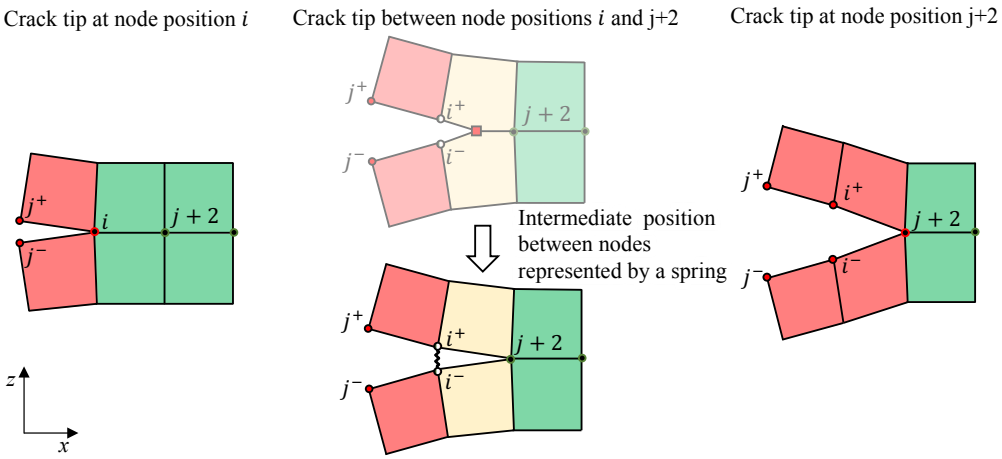

Figure 1: Progressive release procedure and the use of a spring-like kinematic constraint to represent intermediate crack positions.

The present section provides a detailed overview of the procedure used to determine the ERR for unreleased and partially released nodes in a general form suitable for arbitrarily shaped crack fronts. The expressions presented assume regular meshes of brick elements.

2.1. Unreleased and partially released nodes

The Mode I/II/III ERR components for node i in Fig. 1 are determined by:

$$\widetilde{G}_I = \frac{F_z^i \delta_z^j + F_z^{j+2} \delta_z^i}{2A^i} \tag{1}$$

$$\widetilde{G}_{II} = \frac{F_x^i \delta_x^j + F_x^{j+2} \delta_x^i}{2A^i} \tag{2}$$

$$\widetilde{G}_{III} = \frac{F_y^i \delta_y^j + F_y^{j+2} \delta_y^i}{2A^i} \tag{3}$$

in which F_n^k and δ_n^k are the force and displacement jump (difference between the displacement of the top and bottom surfaces), respectively, computed at node pair k along direction n, and A^k is the area associated with node k. The expression for A^k is provided in the following section. Equations 1 to 3 enable the determination of ERR for partially released nodes explicitly. In both [19] and [21], the ERR of partially released nodes was implicitly determined via the assumed unloading curve. Equations 1 to 3 reduce to the classic VCCT expressions, see [2, 3], if the node being considered, in this case node i, has not yet started to release and hence $\delta_{x_{max}}^i = \delta_{y_{max}}^i = \delta_{z_{max}}^i = 0$. As in [2, 3], Eqs. 1 to 3 assume the element size is approximately the same at the front and wake of the crack.

2.2. Arbitrarily shaped crack fronts

The procedure proposed for determining the ERR for a node at an arbitrarily shaped delamination front has two new key features, compared to [19, 21]. The first is that intermediate crack positions, represented by partially released nodes, are explicitly determined and used for estimating the actual crack front shape. The second is that the local crack direction is not assumed but instead estimated as part of the calculation of the ERRs.

The VCCT Eqs. 1 to 3 are derived based on a self-similar crack growth assumption. From an application perspective, this assumption does not impose a limitation on the accuracy of the method and its mesh objectivity. In general, if the crack shape or ERR change dramatically with crack length, one can refine the mesh as required. Furthermore, in propagation simulations, since the self-similar growth assumption is only used locally (in each ERR calculation), the approach tends to self-correct as

the crack propagates, enabling non-self-similar crack growth to be predicted, as will be demonstrated later in this study, e.g. Fig. 16. However, when using Eqs. 1 to 3 to estimate ERR, the displacements, area and force should adhere, as closely as possible, to the self-similar growth assumption used when deriving 1 to 3.

Consider a crack front with an arbitrary shape as illustrated in Fig. 2a, where node i is not yet released and the two adjacent nodes along the crack front have been partially released. To apply Eqs. 1 to 3, one needs to determine the position where displacements should be extracted and their magnitude, as well as the area associated with the release of node i, such that the assumption of local self-similar growth is preserved as closely as possible. Adjacent nodes j to $j+3$ are referred to as "antenna" nodes, following the nomenclature in [14, 19]. The procedure is exemplified using the antenna node j. In general, this procedure should be repeated for all antenna nodes $j+1$ to $j+3$ that are completely released (if any). The ERR at node i is then assumed to be the maximum of the tentative ERRs associated with each antenna node. The progressive nodal release is defined by the crack position d, as will be discussed in Section 3, and is available for all node pairs at the crack front. The crack front position can be estimated based on the values of normalized crack position d at neighboring nodes. An idealized crack front shape, based on the estimation of the crack front position using d, is illustrated in Fig. 2a. The normalized crack position of a node $j+3$, d^{j+3}, see Fig. 2a, can be defined as the cracked length along an edge connecting adjacent node pairs, a_{acc}^{j+3}, divided by the distance between node pairs, a_l; hence $d^{j+3} = \frac{a_{acc}^{i}}{a_l}$. Knowing d^{j+3} and the position, $\mathbf{x}^{j+3}$, of the node $j+3$, the crack position, $\widetilde{\mathbf{x}}^{j+3}$, associated with node $j+3$ can be determined by adding $d^{j+3}a_l$ along the edge defined by the nodes i and the antenna node j being considered in this case. This procedure is repeated any partially released nodes at the crack front. The angles γ and β are defined as the angles between the mesh lines connecting $\mathbf{x}^i$ to $\mathbf{x}^{j+1}$ and $\mathbf{x}^{j+3}$ and the lines connecting the crack position associated with node i, $\mathbf{x}^i$ in Fig. 2a, to the crack positions along adjacent mesh lines, $\widetilde{\mathbf{x}}^{j+1}$ and $\widetilde{\mathbf{x}}^{j+3}$ in Fig. 2a.

The next steps are to determine: (i) the tentative projection of the crack front that ensures the complete release of node i for the various assumed crack growth directions $\mathbf{r}^i$, and (ii) the correspondent wake position that would provide an estimate for the displacement jump registered at nodal position

i if the crack advanced along the direction $\mathbf{r}^i$ (see Figs. 3a and 3c) while preserving its shape. These projections are illustrated in Figs. 3a and 3c as a green dotted line for the tentative projections of the crack front position associated with node i and a red dashed line for the correspondent wake positions. The red dotted line and green dashed line are defined by the angles γ_{fw} and β_{fw}, considered to be positive as depicted in Fig. 3b. The angles γ_{fw} and β_{fw} are assumed to be equal to angles γ and β if these are positive. However, if the angles γ and β are negative, the angles γ_{fw} and β_{cw} and respective green and red lines are not defined, limiting the range of directions that can be sampled, see Fig. 3d. Indeed, in the case where either γ or β are negative, ensuring the complete release of node i would require that the projection of the crack position associated with node i would lay outside the four elements neighboring node i, which has not been pursued in the present study. With this definition of γ_{fw} and β_{fw}, and assuming the crack preserves its shape, the tentative projections of the crack position at node i ensure the complete release of node i such that the overall crack front projection intersects node $j+2$ for the various assumed crack growth directions $\mathbf{r}^i$ as illustrated in Fig. 3. The following step is to define a range of tentative crack direction vectors $\mathbf{r}^i$ with direction given by the angle Ω, Fig. 3. The magnitude of $\mathbf{r}^i$, passing through node i, is determined by considering the origin of $\mathbf{r}^i$ lies at a point along the red dotted line and that it terminates at a correspondent point along the green dashed line. The value $|\Omega_{max}| = 45°$ is used in the present study, limiting the range of tentative directions tried with each antenna node. This avoids redundancy in the calculation of ERRs when using regular meshes, since the procedure is repeated for the other antenna nodes $j+1$ to $j+3$. A detailed discussion on the effect of Ω_{max} and the overall effect of considering multiple tentative crack directions in the ERR calculations is presented in Section 4. The ERR is calculated, for each tentative direction $\mathbf{r}^i$, using the VCCT expressions given in Eqs. 1 to 3. The force $\mathbf{f}^i$ is obtained at node i, while the displacement jump $\boldsymbol{\delta}^j$ is replaced by $\boldsymbol{\delta}^{j*}$ obtained via interpolation using the element's shape functions at a location j^*. Self-similar growth is assumed by considering that the local crack front shape is preserved as the crack advances along a tentative crack direction $\mathbf{r}^i$ to a crack front position that leads to the complete release of node i. With this assumption, the displacement jump that will be registered at node i can be approximated by the displacement at a correspondent crack wake position j^* (along the red dotted line). An area A^i consistent with this crack advancement definition, and that

ensures the applicability of Eqs. 1 to 3, can be estimated by:

$$A^i = \frac{\mathbf{r}^i \times \mathbf{c}^{i,j+1} + \mathbf{r}^i \times \mathbf{c}^{i,j+3}}{4} \tag{4}$$

where the vectors $\mathbf{c}^{i,j+1}$, $\mathbf{c}^{i,j+3}$ define the local crack front shape and are given for Fig. 3b by:

$$\mathbf{c}^{i,j+1} = \widetilde{\mathbf{x}}^{j+1} - \mathbf{x}^i \tag{5}$$

$$\mathbf{c}^{i,j+3} = \widetilde{\mathbf{x}}^{j+3} - \mathbf{x}^i \tag{6}$$

where $\mathbf{x}^i$ is the position of node i and $\widetilde{\mathbf{x}}^{j+1}$ and $\widetilde{\mathbf{x}}^{j+3}$ are the crack front positions associated with nodes $j+1$ and $j+3$, respectively. In this case, the second term in Eqs. 1 to 3 is zero since node i has not started to release yet, hence $\boldsymbol{\delta}^i = 0$. While the procedure is generically illustrated for the node pair i, j, it is repeated for all nodes $j+1$ to $j+3$ that have been completely released. The ERR and crack direction are assumed to correspond to the maximum ERR computed for the various tentative crack directions associated with all antenna nodes. Finally, Fig. 4 illustrates the calculations performed for a case where node i has been partially released. In this case, the virtual position associated with node i is taken into account when determining γ and β and hence γ_{fw} and β_{fw}. The remaining calculation follows the description outlined previously. Likewise, in this case, the displacement jump is obtained at a tentative crack position j^* via interpolation using the element's shape functions. The vector $\mathbf{r}^i$ and area A^i are approximated in a similar fashion, using Eqs. 4 to 6, in which $\mathbf{x}^i$ is replaced by $\tilde{\mathbf{x}}^i$. However, the second term in Eqs. 1 to 3 may be nonzero since node i has started to release; hence $\boldsymbol{\delta}^i$ may not be zero.

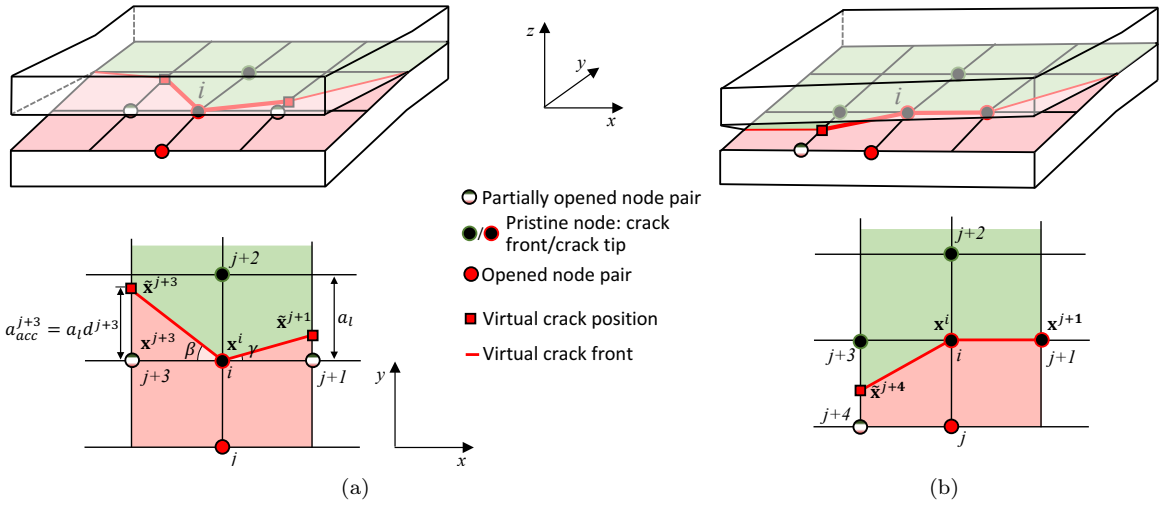

Figure 2: 3D and corresponding plane illustration of two different crack fronts: (a) convex, (b) concave.

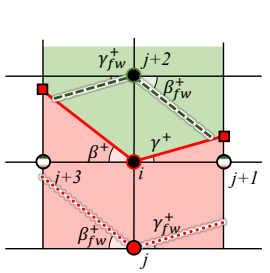

(a) Projections of crack position associated with node i and corresponding wake.

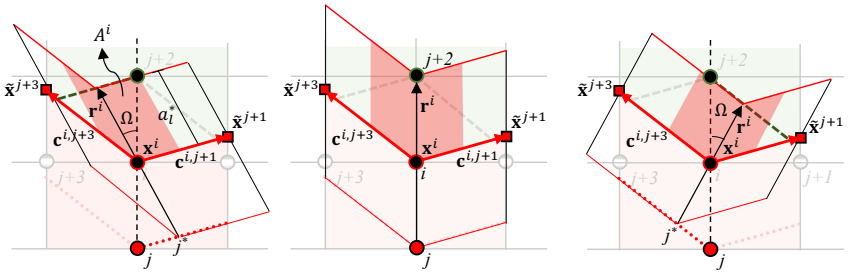

(b) Tentative crack directions r^i and associated area A^i.

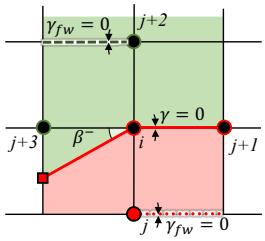

(c) Projections of crack position associated with node i and corresponding wake.

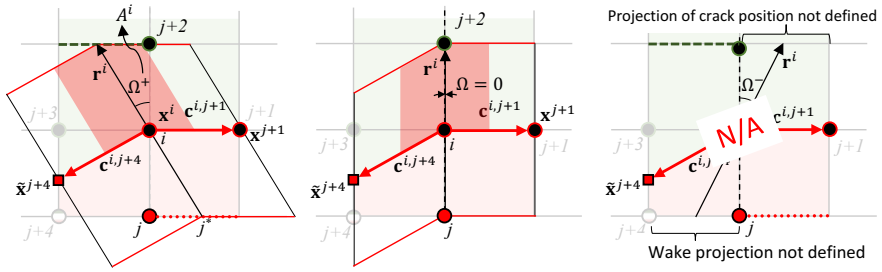

(d) Tentative crack directions r^i and associated area A^i.

Figure 3: Illustration of the calculation of the displacement jump extraction location j^* and the area A^i for multiple tentative crack directions. (a) and (b) convex case in Fig. 2a, (c) and (d) concave case in Fig. 2.

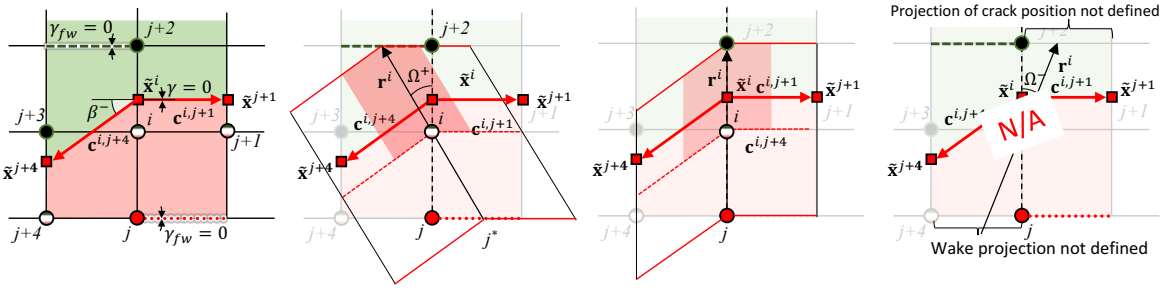

(a) (b)

Figure 4: Illustration of the calculation of the displacement jump extraction location j^* and the area A^i for multiple tentative crack directions in a case where node i is partially released.

3. Simulating fatigue crack growth via progressive nodal release

In the present study, the progressive release algorithm is implemented using Floating Node Method (FNM) [22] concepts as illustrated Fig. 5. A 3D solid continuum brick FNM element, fully integrated, comprising twelve real nodes and four floating nodes, was implemented. The twelve real nodes are used to model the interface and the material above and below it, as shown in Fig. 5a. Before the interface is delaminated, the floating nodes are not used. As the interface delaminates, the floating nodes are used as required to represent the delaminated interface, see Fig. 5b. This strategy avoids the use of duplicate nodes held by high penalty stiffness springs, to represent regions of the interface that did not yet delaminate [19]. However, the progressive release procedure and accompanying calculations are applicable in general and do not require the use of the FNM. The present section provides a detailed description of the progressive release procedure.

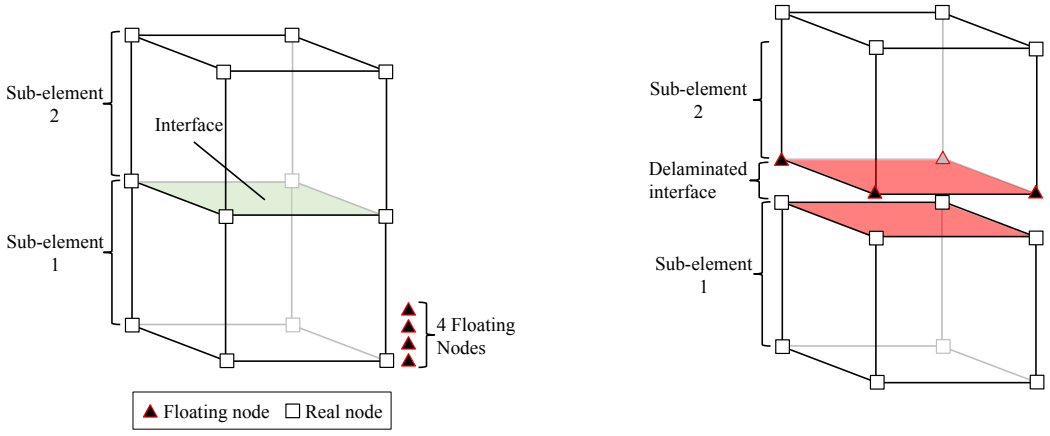

(a) Split FNM element to model a generic interface $0/\theta$.

(b) Fully delaminated element

Figure 5: Floating Node Method element.

Consider a pure mode I loading, i.e., $G_I = G_T$ and assume that node i is at the crack front as shown in Fig. 1. The ERR associated with node i is given by Eq. 1 and can be written simply as:

$$\widetilde{G}_I = \frac{F^i_{z_{max}} \delta^j_{z_{max}}}{2A^i} \tag{7}$$

since node i is at the crack tip and hence $\delta^i_{z_{max}} = 0$. Let us now assume the crack starts growing past node i to an intermediate location between node i and the next node position $(j+2)$. For a linear elastic case, assuming self-similar conditions as the crack propagates, the force $F^i_{z_{max}}$, from Eq. 8, is assumed to decrease linearly:

$$F^i_z = F^i_{z_{max}} \left(1 - \frac{\Delta A}{A^i}\right) = F^i_{z_{max}} (1 - d) \tag{8}$$

where ΔA represents an intermediate crack position. The normalized crack position $d \in [0, 1]$ is defined as $d = \frac{\Delta A}{A^i}$, such that if $d = 1$ the node is completely released, and the force F^i_z at the node pair i reduces to zero. Using the same assumptions, a relationship similar to Eq. 8 can be written for the displacement jump:

$$\delta^i_z = \delta^i_{z_{max}} d \tag{9}$$

where δ^i_z is the displacement jump at node position i, which will equal $\delta^j_{z_{max}}$ when the node pair is completely released. Alternatively, the relationships given in Eq. 8 and 9 can be combined and written as:

$$F^i_z = m_z \delta^i_z + F^i_{z_{max}} \tag{10}$$

where $m_z = -\frac{F^i_{z_{max}}}{\delta^j_{z_{max}}}$. For a given value d, Eq. 10 can also be written as:

$$F^i_z = k_z \delta^i_z = m_z \left(1 - \frac{1}{d}\right) \delta^i_z \tag{11}$$

and hence the stiffness of the spring k_z between node pair i^+ and i^- can be expressed as:

$$k_z = m_z \left(1 - \frac{1}{d}\right) \tag{12}$$

and Eq. 11 can be generally written for all degrees of freedom as:

$$\mathbf{f}^i_{VCCT} = \mathbf{M} \left(1 - \frac{1}{d}\right) \boldsymbol{\delta}^i \tag{13}$$

where:

$$\mathbf{M} = \begin{bmatrix} m_x & 0 & 0 \\ 0 & m_y & 0 \\ 0 & 0 & m_z \end{bmatrix} \tag{14}$$

In Figs. 6a and 6b, the relationships given by Eqs. 10 and 11 are represented graphically for z and x directions. Both $F^i_{l_{max}}$ and $\delta^j_{l_{max}}$ are typically different for each direction $l = \{x, y, z\}$ leading to different slopes of the unloading curves, as illustrated in Fig. 6. Assume that conditions change during the progressive release, and the updated $\widetilde{G_I}^{new}$, $\widetilde{G_{II}}^{new}$ are different from the initial $\widetilde{G_I}$, $\widetilde{G_{II}}$ that led to a finite amount of growth, illustrated in Figs 6c and 6d. This can occur as the crack propagates in a non-self-similar fashion as a result of unloading after some initial release and re-loading with different loading conditions. Despite the different loading conditions, if no growth occurs during unloading and re-loading according to the fracture criterion/growth law assumed, the spring stiffnesses, k_z^U and k_z^R :

$$k_z^U = m_z^U \left(1 - \frac{1}{d^U}\right) \tag{15}$$

$$k_z^R = m_z^R \left(1 - \frac{1}{d^R}\right) \tag{16}$$

where the superscripts U and R designate variables associated with unloading (U) and re-loading (R), should be identical and equal to k_z:

$$k_z^U = k_z^R = k_z \tag{17}$$

In addition, since no growth occurs:

$$d^U = d^R = d \tag{18}$$

Recalling Eq. 11, Eqs. 17 and 18 are satisfied if:

$$m_z^U = m_z^R = m_z \tag{19}$$

and thus m_z is considered constant during the progressive release. Using similar arguments, m_x and

m_y are also considered constant during the progressive release. This guarantees that no artificial crack healing or crack growth occurs as a result of variation of loading conditions without a fracture criterion or growth law being met.

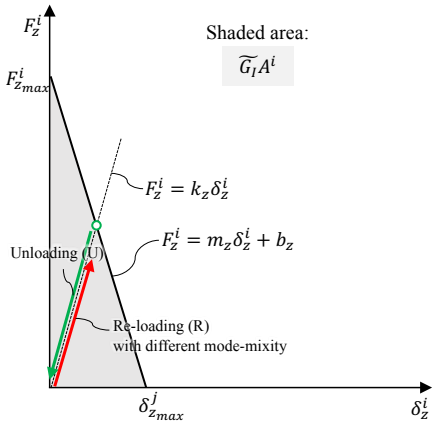

(a) Mode I progressive release curve (z-direction). Unloading and re-loading should follow the same slope.

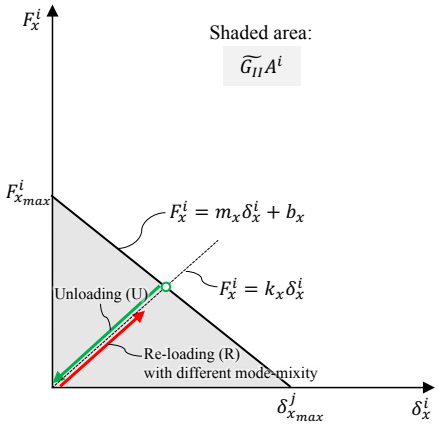

(b) Mode II progressive release curve (x-direction). Unloading and re-loading should follow the same slope.

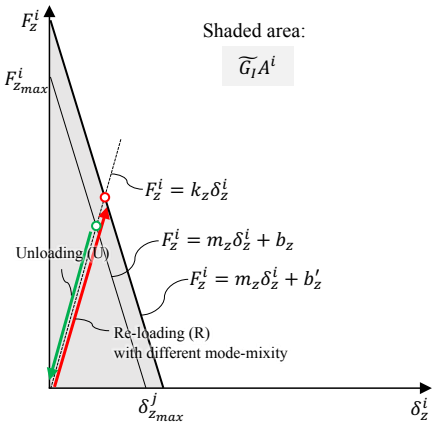

(c) Updated (shifted) Mode I progressive release curve upon re-loading as a result of a change in loading conditions, (z-direction).

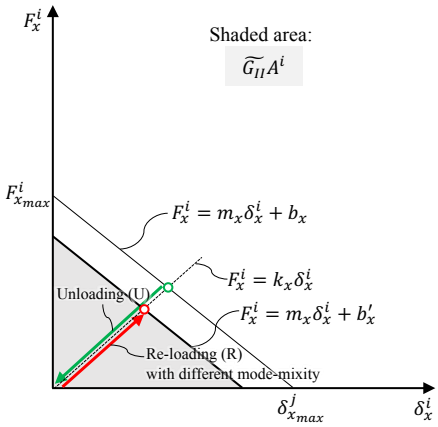

(d) Updated (shifted) Mode II progressive release curve upon re-loading as a result of a change in loading conditions, (x-direction).

Figure 6: Variation of the progressive release relationships as a consequence of a change in mode-mixity due to unloading and re-loading with different loading conditions.

3.1. Fatigue crack growth

For simplicity, let us assume the growth rate at each node i can be given by an exponential expression of the type:

$$\left(\frac{\mathrm{d}a}{\mathrm{d}N}\right)^{i} = C\left(G^{i}_{T_{max}}\right)^{n} \tag{20}$$

similar to a Paris-Law, where C and n are determined experimentally. Note that C and n can also be a function of mode-mixity or other variables and hence can be different for each node i. For the purpose of the subsequent explanation, C and n are assumed constant. Indeed, other expressions for $\frac{\mathrm{d}a}{\mathrm{d}N}$, such as provided in [23, 24], can also be used. Knowing the growth rate $\left(\frac{\mathrm{d}a}{\mathrm{d}N}\right)^{i}$, it is possible to estimate the number of cycles needed for the crack to propagate by a fraction $0 < \lambda \leq 1$ of the length that would lead to complete nodal release a^{i}_{l*} :

$$\Delta N^{i}_{\lambda} = \frac{\lambda a^{i}_{l*}}{\left(\frac{\mathrm{d}a}{\mathrm{d}N}\right)^{i}} \tag{21}$$

The fraction λ designates the "crack growth increment". In the present study, λ was defined globally for simplicity. A local definition for λ may be more appropriate, for cases where dissimilar element sizes may be present. Additionally, the cycles needed for the crack to propagate to the next nodal position are also computed:

$$\Delta N^{i}_{a_l} = \frac{a^{i}_{l*}\left(1-d^{i}\right)}{\left(\frac{\mathrm{d}a}{\mathrm{d}N}\right)^{i}} \tag{22}$$

where:

$$d^{i} = \frac{a^{i}_{acc}}{a^{i}_{l*}} \tag{23}$$

and a^{i}_{acc} represents the accumulated crack growth. Subsequently, for each node i at the crack front, ΔN^{i} is determined:

$$\Delta N^{i} = \min\left\{\Delta N^{i}_{\lambda}, \Delta N^{i}_{a_{l*}}\right\} \tag{24}$$

where ΔN^{i} is the minimum number of cycles needed to either propagate the crack by the set increment length λa^{i}_{l*} or to grow it to the next nodal position. Subsequently the minimum of all ΔN^{i} determined

for each node i along the crack front is computed:

$$\Delta N_{inc} = \min\left\{\Delta N^1, ..., \Delta N^i, ..., \Delta N^m\right\} \tag{25}$$

where the superscript m designates the total number of nodes at the crack front. Further, it is assumed that, in this increment, all nodes at the crack front are fatigued by ΔN_{inc} cycles. This ensures that the set crack increment $\lambda a^i_{l^*}$ is not exceeded anywhere in the model and that the crack does not accumulate beyond $a^i_{l^*}$ such that at any time $d^i \leq 1$. Knowing ΔN_{inc}, the increment Δd^i can be computed by:

$$\Delta d^i = \frac{\left(\frac{\mathrm{d}a}{\mathrm{d}N}\right)^i \Delta N_{inc}}{a^i_{l^*}} \tag{26}$$

and the updated d^i_{new} can be computed as:

$$d^i_{new} = d^i + \Delta d^i \tag{27}$$

A node initiates its progressive release when:

$$d^i_{new} > \zeta \tag{28}$$

The value for ζ does not affect the solution, provided ζ is sufficiently small. In this study, it is assumed $\zeta = 0.001$. However, not defining ζ may lead to convergence issues due to very high stiffnesses k being computed at the onset of the progressive release for very small d^i_{new}, see Eq. 12. Finally, a node is considered to completely release when:

$$d^i_{new} = 1 - \xi \tag{29}$$

The tolerance ξ provides a measure of the accumulation of crack growth required before a node is completely released. By increasing the tolerance ξ, more nodes will be released per increment, accelerating the analysis at the expense of a coarser solution. The effects of varying tolerance ξ will be discussed further in Section 4.

3.2. Equilibrium Equations

Consider the equilibrium of a generic linear elastic solid of volume Ξ subject to external forces, $\mathbf{f}_{ext}$, with internal stresses, $\boldsymbol{\sigma}$, in which partially released springs, $\mathbf{f}_{VCCT}(\boldsymbol{\delta})$, are included to represent intermediate crack positions:

$$\int_{\Xi} \boldsymbol{\sigma} \mathrm{d}\Xi + \mathbf{f}_{VCCT}(\boldsymbol{\delta}) + \mathbf{f}_{ext} = 0 \tag{30}$$

Using the principal of virtual work, and recalling Eq. 13:

$$\int_{\Xi} \mathbf{B}^t \mathbf{C} \mathbf{B} \mathbf{u} \mathrm{d}\Xi + \underbrace{\mathbf{D}^t \mathbf{M} \left(1 - \frac{1}{d}\right) \mathbf{D}\mathbf{u}}_{\mathbf{f}_{VCCT}} + \mathbf{f}_{ext} = 0 \tag{31}$$

where $\boldsymbol{\varepsilon} = \mathbf{B}\mathbf{u}$, $\boldsymbol{\sigma} = \mathbf{C}\boldsymbol{\varepsilon}$ and $\boldsymbol{\delta} = \mathbf{D}\mathbf{u}$. Following the procedure outlined in the previous section, d is updated at the end of each converged increment leading to an explicit crack propagation. In this case, Eq. 31 is linear and easily solvable. The explicit crack propagation used in this study leads to a linear system of equations and hence no convergence difficulties.

3.3. Implementation

This section provides an overview of how the approach is implemented. The method is implemented in Abaqus/Standard® via the user element depicted in Fig. 5. As mentioned previously, different forms of the element may be acceptable, e.g. [19], and combined with the progressive release algorithm proposed. Although not pursued at this time, the application and extension of the methodology to other element types, such as prisms or tetrahedrons, is considered of interest. Additionally, the optimization of the algorithm to accommodate transition regions from fine to coarse meshes and/or distorted elements has also not been pursued.

The present algorithm assumes that the growth rate $\frac{\mathrm{d}a}{\mathrm{d}N}$ is written as given in Eq. 20. Other functional forms for $\frac{\mathrm{d}a}{\mathrm{d}N}$, (see [23]), may require modifications to the algorithm, including additional finite element analysis. The proposed algorithm is event-based, where an event is defined as a growth increment or a node being completely released, or both. Therefore, the number of cycles is calculated as a function of the assumed growth increment as part of the solution. The event-based algorithm is

chosen for illustrative purposes; however, other algorithms, such as cycle-based, could also be explored using the same overall methodology. In such a case, a fixed number of cycles is assumed, and the corresponding growth increment is calculated as part of the solution. In the present implementation, the solution is obtained as follows:

1. An implicit finite element analysis is performed, through which nodal forces and displacements are obtained for all nodes at the crack front (Eq. 31). The ERRs are determined using Eqs. 1 to 3 and the procedure outlined in Section 2.
2. Once the ERR at each node is known, the growth rate can be determined, (Eq. 20).
3. The cycle increment, ΔN_{inc}, is computed, (Eq. 25).
4. The incremental crack growth for each node i at the front, Δd^i, is computed using Eq. 26 and accumulated via Eq. 27, obtaining an updated d^i_{new}.
5. d^i_{new} is set to 1 for all nodes at the crack front for which Eq. 29 is satisfied.
6. All nodes that satisfy Eq. 28 initiate their progressive release.
7. The total cycle count is updated, $N_{Total} = N_{Total} + \Delta N_{inc}$, and the procedure is repeated.

In the present Abaqus/Standard® implementation, the calculation of ERRs is performed externally to the user element via a python script. The information from the user elements, namely displacements and forces, is passed to the python script via an Abaqus/Standard® user subroutine `UEXTERNALDB.f` and auxiliary text files.

4. Results

The present section starts with a description of the finite element models used to assess the methodology proposed, (Section 4.1). This assessment focuses first on the ERR calculation and in particular on the effect of Ω_{max}, (Section 4.2). Subsequently, the results obtained from the verification of the propagation algorithm for Mode I, including a brief sensitivity study, are provided in Section 4.3. These are followed by the verification results for mixed-Mode I/II and Mode II, Sections 4.4 and 4.5, respectively. This section concludes by reporting results from verification exercises which evaluate the suitability of the algorithm to capture the propagation of arbitrary crack shapes that do not conform to the underlying mesh (Section 4.6).

4.1. Finite element models

Finite element models of the Double Cantilever Beam (DCB), Mixed Mode Bending (MMB), and End Notch Flexure (ENF) test specimens were built and are shown in Fig. 7. These models are used to verify the approach proposed for mode-mixity ranging from pure Mode I to pure Mode II. Dimensions, mesh refinement, boundary conditions and material properties are based on those used in the benchmarks given in [8, 25, 26] so that the accuracy of the proposed approach can be assessed by comparison to the benchmarks. The material properties are summarized in Tables 1 to 3. In addition, to assess the ability of the approach to model the growth of delaminations with arbitrary shapes, simulations of an elliptical and a circular planar crack under uniform cyclic tension and shear were performed. The initial shapes are approximately prescribed following the mesh lines and hence are not smooth. The models used are illustrated in Figure 8. The solid is considered to be made of an isotropic material with Young's modulus $E = 7000\,\text{GPa}$ and Poisson ratio $\nu = 0.33$, and the Paris Law coefficient and exponent are assumed as given in Table 1. This exercise is based on a similar verification study performed in [13]. In both cases, the cracks are assumed to remain planar as they propagate.

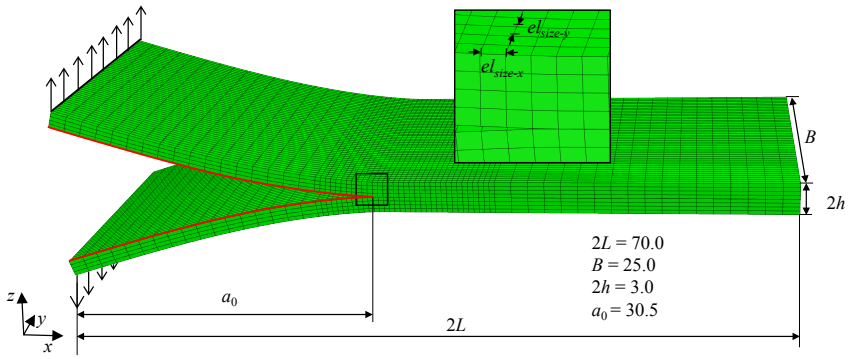

(a) DCB

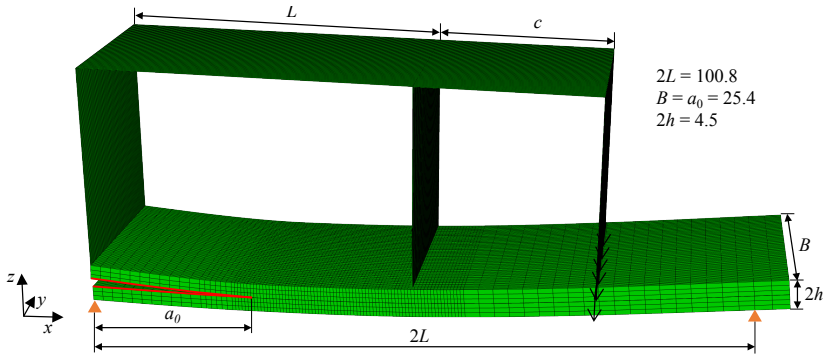

(b) MMB. The mode ratios $\beta = \{0.2, 0.5, 0.8\}$, correspond to $c = \{92.7, 41.3, 29.2\}$.

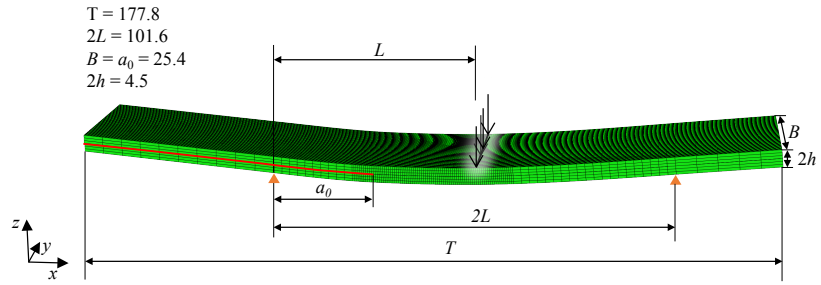

(c) ENF

Figure 7: DCB, MMB and ENF models. Dimensions, mesh and boundary conditions based on [8, 25, 26]. All dimensions shown are in mm.

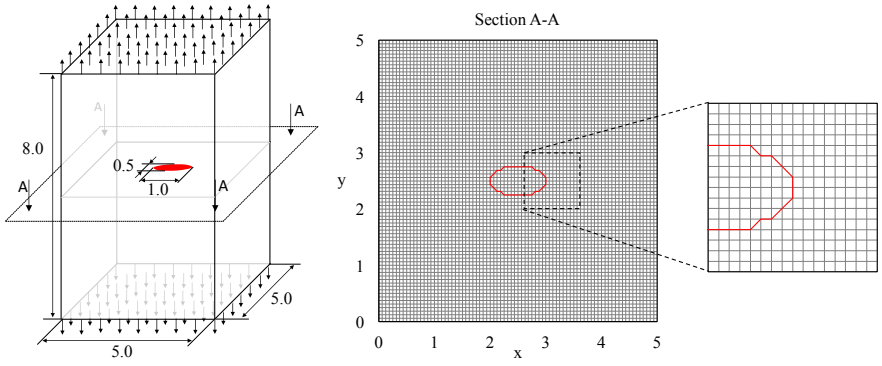

(a) Uniform tension

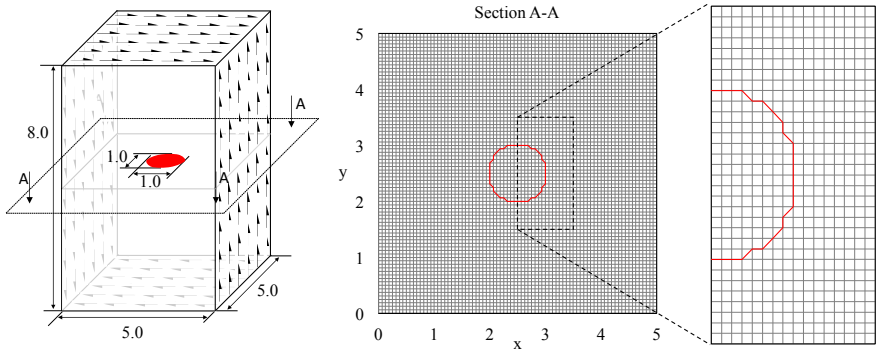

(b) Uniform shear

Figure 8: Numerical model of an isotropic solid with (a) embedded elliptical crack under uniform tension, (b) embedded circular crack under uniform shear. Mesh sizes are illustrated as well as the initial cracks and how they conform to the underlying mesh. All dimensions are given in mm.

Table 1: Elastic properties, and Paris law coefficient C in $\frac{\text{mm}}{\text{cycle}}\left(\frac{\text{kJ}}{\text{mm}}\right)^{-n}$ and exponent n used in the DCB benchmark [25].

E_{11} (GPa)	$E_{22} = E_{33}$ (GPa)	$\nu_{12} = \nu_{13}$	ν_{23}	$G_{12} = G_{13}$ (GPa)	G_{23} (GPa)	C	n
139.4	10.16	0.3	0.44	4.6	3.99	2.44×10^6	10.61

Table 2: Elastic properties used in the MMB and ENF benchmarks [8, 26].

E_{11} (GPa)	$E_{22} = E_{33}$ (GPa)	$\nu_{12} = \nu_{13}$	ν_{23}	$G_{12} = G_{13}$ (GPa)	G_{23} (GPa)
161	11.38	0.32	0.44	5.17	3.98

Table 3: Paris law coefficient C in $\frac{\text{mm}}{\text{cycle}}\left(\frac{\text{kJ}}{\text{mm}}\right)^{-n}$ and exponent n used in the MMB and ENF benchmarks as a function of mode-mixity β [8, 26].

	$\beta = 0.2$	$\beta = 0.5$	$\beta = 0.8$	$\beta = 1.0$
C ($\frac{\text{mm}}{\text{cycle}}\left(\frac{\text{kJ}}{\text{mm}}\right)^{-n}$)	2412	6.79	4.58	0.33
n	8.4	5.4	4.1	5.55

4.2. Effect of Ω_{max} on energy release rate calculation and crack propagation

The value of Ω_{max}, as defined in Section 2.2, provides an upper bound to the tentative local crack directions along which the ERR is computed. In this section, the effect of Ω_{max} on the ERR calculation is illustrated. Scaled versions of the DCB (Mode I) and ENF (Mode II) models in Fig. 7 were built. Contrary to the models presented in Fig. 7, the width of the models used in this section was reduced to $B = 2\,\text{mm}$, and the number of elements along the width was reduced to four.

To assess the effect of Ω_{max} in the ERR calculation for each model, two initial crack front shapes were considered: (a) straight crack front and (b) chevron crack front obtained by completely releasing the central node of the straight crack front. For each crack front, ERRs were determined as a function of $|\Omega_{max}|$ which varied between 0° and 45° in 15° increments. When applied along a crack front that has not yet started to release, the ERRs determined by the proposed algorithm, assuming $\Omega_{max} = 0$, are expected to provide similar results to those obtained with the procedures used in [19–21]. In [19–21], ERRs are determined from the forces at node i and the displacement jumps at the four antenna nodes (along mesh lines). The upper limit, 45°, was chosen since for square meshes $|\Omega_{max}| > 45^\circ$ results in redundant values of ERRs being calculated. The results obtained are illustrated in Fig. 9, in which additional results from equivalent models built with Abaqus/Standard® native C3D8I elements are also included. As can be seen in Fig. 9a for straight cracks, the ERRs along the crack front do not seem to vary as a function of Ω_{max}. However, in Fig. 9b, it is clear that the ERRs computed at the nodes immediately adjacent to the central node tend to increase with Ω_{max}. In the DCB case, the ERR of the nodes adjacent to the central node is always larger than the ERR at the central node. This indicates that the adjacent nodes would initiate their release before the central node, which would tend to smooth the chevron crack shape. However, in the ENF case with $\Omega_{max} = 0$, the ERRs obtained at

adjacent nodes are very similar (smaller for ERRs obtained with Abaqus) than those obtained at the central node. This suggests that the chevron shape would tend to be preserved (or further pronounced) rather than smoothed. Only for values of $\Omega_{max} \geq 30^{\circ}$ does the ERR at the nodes adjacent to the central node become significantly larger than the central node, indicating that the crack would likely tend to become smoother.

The effect of Ω_{max} on delamination propagation was further investigated by using the approach proposed in this study to simulate the propagation of a chevron crack front while assuming different values of Ω_{max}. For each model, DCB and ENF, two simulations were performed assuming $\Omega_{max} = 0$ and $\Omega_{max} = 45^{\circ}$. As can be seen in Fig. 10 in the DCB simulations, the initially prescribed chevron shape smooths after a few increments of growth, and the typical concave (thumbnail) crack shape is obtained regardless of Ω_{max}, with slightly smoother results obtained with $\Omega_{max} = 45^{\circ}$. On the other hand, the ENF simulations show that with $\Omega_{max} = 0$, the chevron crack shape is not smoothed but instead is further pronounced after a few increments of growth to form a zig-zag shape with approximately one element length of amplitude, see Fig. 10. However, if $\Omega_{max} = 45^{\circ}$ is used instead, a smooth convex crack shape, typical of ENF specimens, is obtained after a few increments of growth.

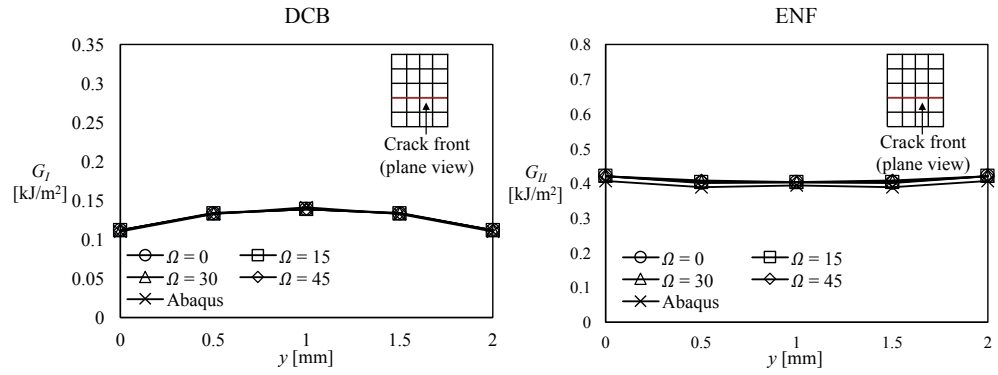

(a) Straight crack

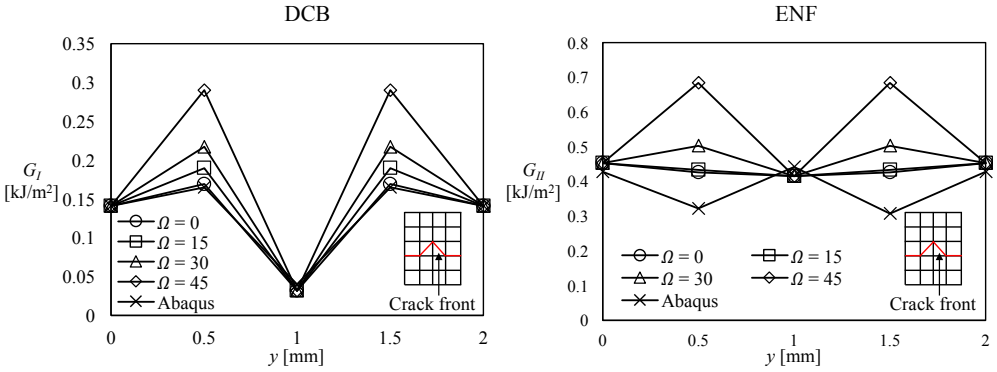

(b) Chevron crack

Figure 9: Energy release rate as a function of Ω_{max} for DCB and ENF

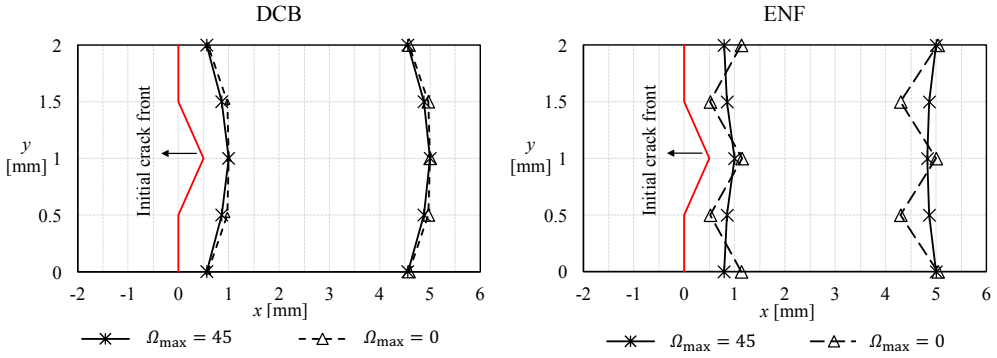

Figure 10: Chevron crack shape growth as a function of Ω_{max} for DCB and ENF

4.3. Mode I (DCB)

In the present section, the ability of the procedure to simulate Mode I delamination growth is assessed using the full scale model (with width B equal to 25 mm) illustrated in Fig. 7a. Mesh size in the refined region was assumed $el_{size-x} = 0.5\,\text{mm}$, $el_{size-y} = 0.5\,\text{mm}$. All simulations reported in the present study were performed with crack growth increment ratio and release tolerance set to $\lambda = 0.2$ and $\xi = 0.025$, respectively, unless otherwise stated. A sensitivity study on the effect of these parameters is presented in the next section. Figure 11a shows that the results obtained compare well with the 2D benchmark from [25]. The discrepancy observed is due to the difference between the ERR obtained with the 2D model used to define the benchmark and the 3D simulation performed in the present study. This was verified by simulating growth while enforcing the crack to remain straight and determining the growth rate at each increment using the ERR computed at the center of the specimen (which approximates the plane strain conditions assumed in the 2D benchmark). The results from this simulation are given in Fig. 11a and labeled "Simulation, quasi-2D". As can be seen, they are nearly identical to the 2D benchmark. Additionally, Fig. 11b shows a planar view of the simulated crack front obtained after a few increments of growth. The gridlines correspond to element boundaries. The thumbnail shape obtained is characteristic of DCB specimens, see e.g. [27]. Note that the crack was initially straight, as highlighted in Fig. 11b. Indeed, Figure 11b indicates that the procedure proposed is capable of accommodating a crack front which does not conform to the underlying mesh and can develop in a mesh-independent fashion. The crack is seen to traverse multiple element boundaries without any marked effect on its smoothness or shape.

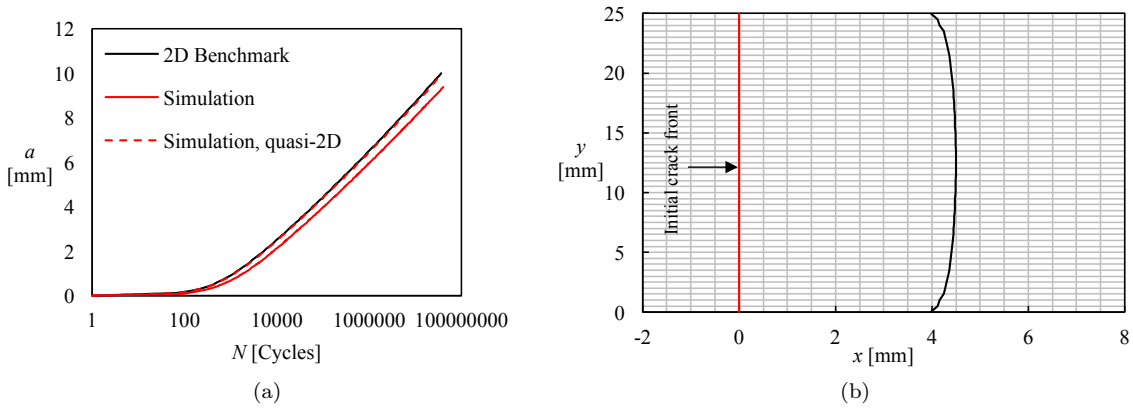

Figure 11: DCB (Mode I) results. (a) crack growth results obtained with the proposed approach compared with the 2D benchmark obtained in [25]; (b) planar view of the crack front as simulated by the present approach that has propagated a maximum of 4.5 mm.

4.3.1. Sensitivity study

In the present section, the ERR calculation and the simulated crack shape are assessed as a function of mesh, crack growth increment λ, and release tolerance ξ.

In Fig. 12, the crack front shape and ERR along the crack front of a DCB specimen are illustrated. Both ERR distribution and crack front shape were obtained for the increment corresponding to a maximum crack growth of 4.5 mm. In this case, progressively finer meshes, with element sizes correspondent to $el_{size} = el_{size_x} = el_{size_y} = \{1.0,\ 0.5\ , 0.25\}$ mm, were used. All meshes used captured the typical thumbnail shape observed in DCB specimens. However, progressively finer meshes led, in general, to a smoother crack front and more pronounced thumbnail shapes, (Fig. 12a), as well as smoother ERR distributions along the crack front, (Fig. 12b).

Both crack increment λ and release tolerance ξ affect the overall smoothness of the solution. Decreasing ξ and/or λ leads to progressively smoother crack front shapes and ERR distributions, at the expense of a larger number of growth increments, and hence longer runtimes. This is illustrated in Fig. 13 by progressively decreasing ξ for a fixed λ. If either value, ξ or λ, is much smaller than the other, it will control the release after the first increments of growth.

The small oscillations in ERR observed, Fig. 12b and 13, are a function of the local crack front smoothness and hence both mesh refinement and crack increment λ. Additionally, they are often

associated with regions where the tolerance ξ is met, leading to a small crack jump. Hence, decreasing mesh size and the crack increment λ, as well as ξ, systematically contributes to a smoother crack front.

In all cases simulated in this study, no convergence difficulties were encountered, independent of chosen values for element size, crack increment λ, and tolerance ξ.

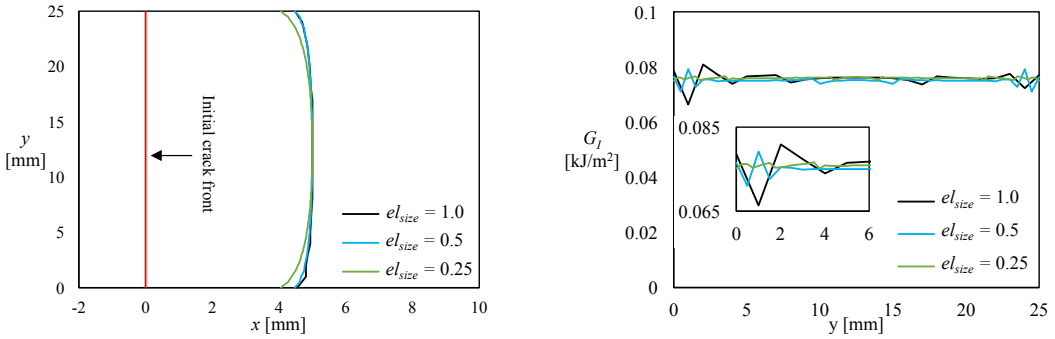

(a) crack position

(b) energy release rate along the crack fronts given in (a) that propagated to $x_{max} = 4.5\,\text{mm}$

Figure 12: Effect of mesh refinement on crack front shape and energy release rate distribution. Results obtained with $\lambda = 0.25$ and $\xi = 0.01$ and $el_{size} = el_{size-x} = el_{size-y}$.

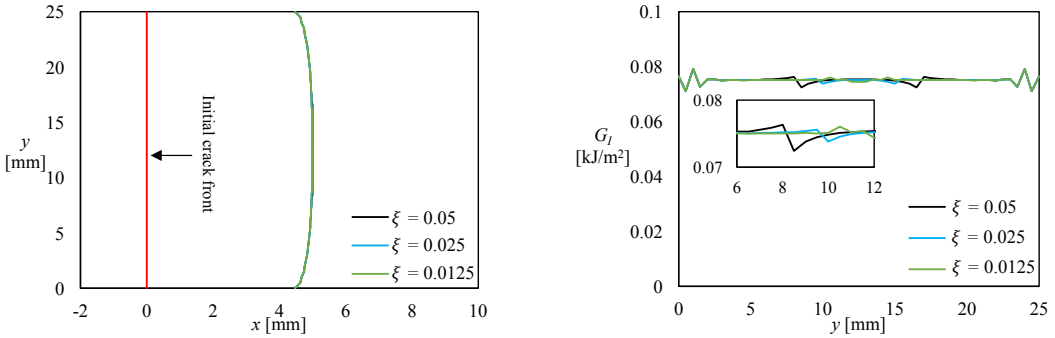

(a) crack shape

(b) energy release rate along the crack fronts given in (a) that propagated to $x_{max} = 4.5\,\text{mm}$

Figure 13: Effect of release tolerance ξ on crack front shape and energy release rate distribution. Results obtained with $el_{size} = el_{size-x} = el_{size-y} = 0.5\text{mm}$, $\lambda = 0.25$.

4.4. Mixed-Mode I/II (MMB)

In this section, results obtained with MMB (Mixed Mode I/II) model, Fig. 7b, are shown and compared to 2D benchmark results [8]. For all cases, the solution parameters were kept constant,

including: mesh size $el_{size-x} = 0.5\,\text{mm}$, $el_{size-y} = 0.5\,\text{mm}$. All cases approximate well the benchmark solution as shown in Fig. 14a. A representative steady state crack shape for $\frac{G_{II}}{G_T} = 0.5$, as determined by the simulations, is shown in Fig. 14b. The crack shape obtained is predominantly straight, as observed experimentally, with slight tendency to become more concave/convex as a function of the the mode-mixity applied.

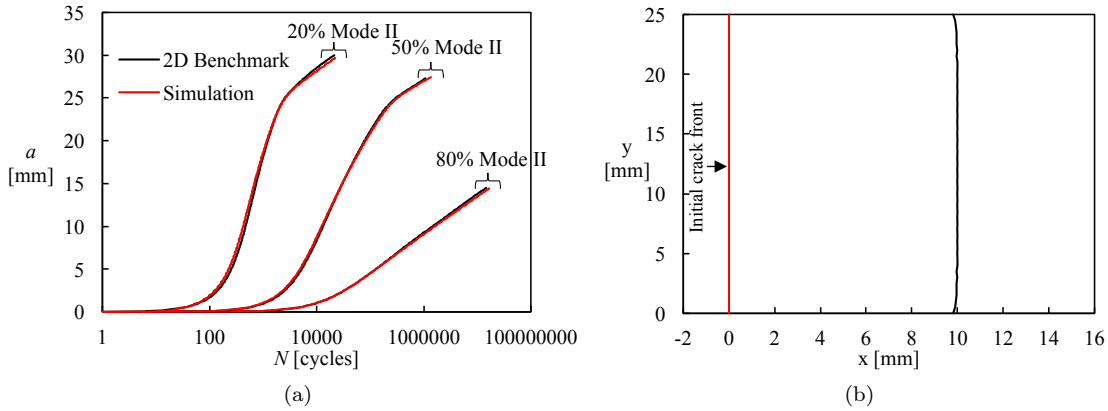

Figure 14: MMB (Mixed Mode I/II) results. (a) crack growth results obtained with the proposed approach compared with the 2D benchmark obtained in [8]; (b) planar view of the crack front simulated by the present approach for $\frac{G_{II}}{G_T} = 0.5$ and a crack which has grown to $x_{max} = 10\,\text{mm}$.

4.5. Mode II (ENF)

The results obtained with the ENF model (Mode II), Fig. 7c, are illustrated in Figure 15. As shown in Fig. 15a, and similarly to what is reported in the previous sections, the crack growth simulation compares well with the respective 2D benchmark from [26]. As in the DCB case, the small discrepancies observed are attributed to the 2D nature of the benchmark when compared with the 3D simulation performed. Note that in both ENF and DCB simulations, the crack front shape departs more from a straight crack front than in the MMB simulations, and hence a larger discrepancy between simulation and benchmark. Figure 15b shows a planar view of the delamination front with three results reported. The convex shape of the crack is typical of ENF specimens. The curve labeled "Present study" corresponds to crack fronts obtained using the approach proposed. The curve labeled "Ref. [21] - no smoothing" was obtained following the approach discussed in [21]. In [21], the ERR

was calculated without accounting for the crack front shape and using only the displacements obtained at antenna nodes j to $j+3$ shown in Fig. 2, without performing any interpolation. In addition, an alternative expression (rather than Eqs. 1 to 3) based on the unloading curve (force-displacement) was used in [21] to determine ERRs in partially released nodes. The results obtained show that a zig-zag crack front with amplitude similar to the element length, in this case $el_{size_x} = 0.5\,\text{mm}$, develops after some crack growth. In [21], this non-physical behavior was alleviated by performing Gaussian smoothing of the crack front after each growth increment. However, the smooth results obtained with the present approach indicate that Gaussian smoothing may not be required if the procedure described in Section 2 is adopted.

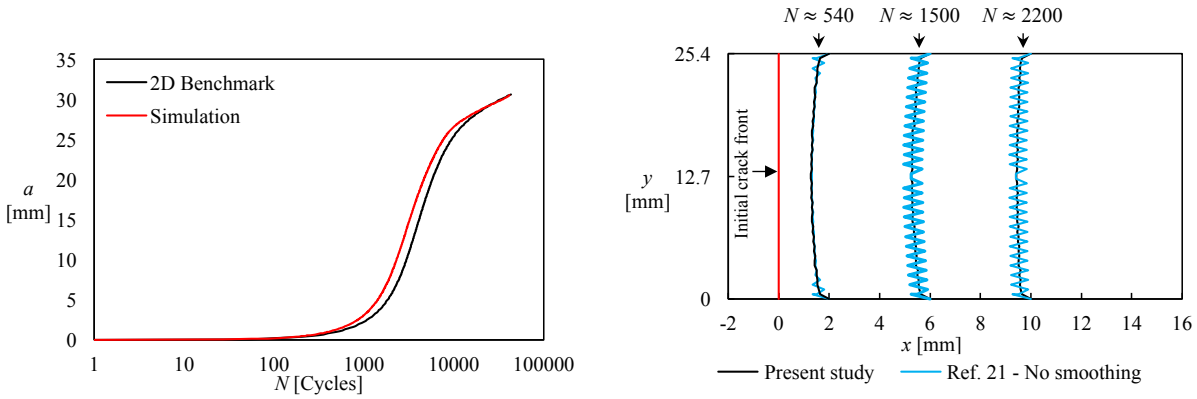

Figure 15: ENF (Mode II) results. (a) crack growth results obtained compared with the proposed approach to the 2D benchmark obtained in [26]; (b) planar view of three different crack front positions comparing the approach proposed in this study with [21].

4.6. Arbitrarily shaped cracks

This section focuses on the qualitative assessment of the method's capability to model growth of delaminations with arbitrary shapes. The first verification exercise consists of an elliptical planar crack embedded in an isotropic solid loaded in uniform cyclic tension, as shown in Fig. 16a. The mesh size used was $el_{size} = el_{size_x} = el_{size_y} = 0.0625\,\text{mm}$, as illustrated in Fig. 8. The results obtained are shown in Fig. 16b. Note that the initial approximate crack shape is prescribed following mesh lines and hence is not smooth. As the crack propagates, smoother shapes are obtained. Different intermediate

shapes can be observed, progressively converging to a circular shape, as expected [13]. The second case corresponds to the same solid but under uniform shear as depicted in Fig. 17a. However, in this case the initial shape, conforming to the underlying mesh, approximates a circle rather than an ellipse. As the crack grows, it smoothly elongates the circle along the axis aligned with the shear loading as expected. It is worth noting that, in either case, the initial un-smooth shape that results from the initial crack conforming to the underlying mesh rapidly evolves to a smooth crack shape after a small number of growth increments.

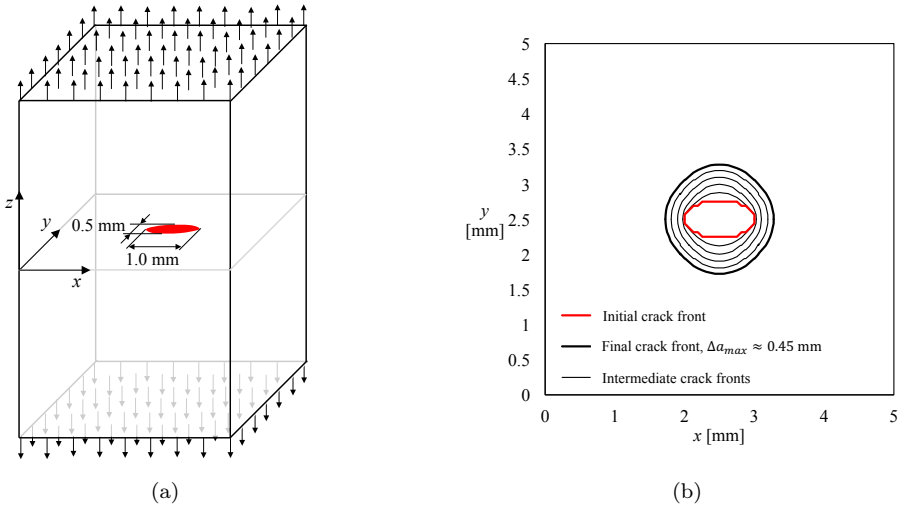

(a) (b)

Figure 16: Embedded elliptical planar crack: uniform tension.

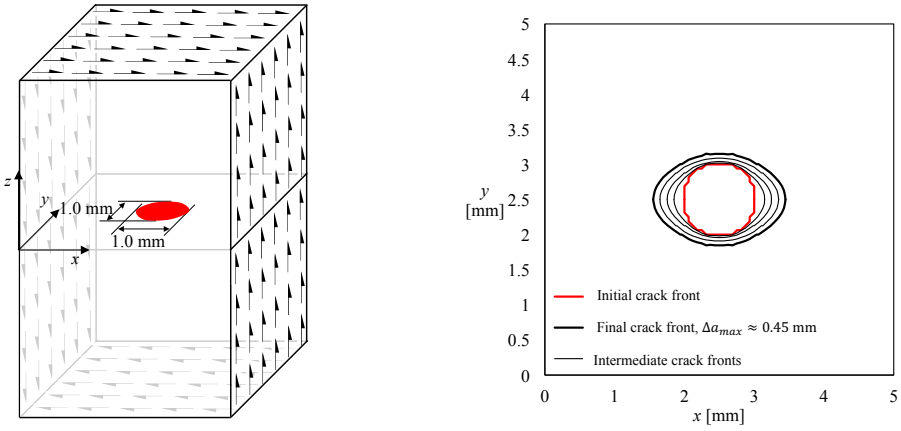

(a) (b)

Figure 17: Embedded circular planar crack: uniform shear.

5. Discussion

Overall, the results obtained in the previous section show good quantitative agreement between the simulation method and 2D benchmarks obtained for DCB (Mode I), MMB (Mixed Mode I/II) and ENF (Mode II) specimens. Also, qualitatively, the crack shapes typical of the characterization specimens were successfully captured, e.g. thumbnail shape in the DCB specimen and opposed thumbnail shape in the ENF specimen. Additionally, the simulations of planar growth of embedded circular and elliptical cracks in an isotropic solid demonstrate that the method is capable of successfully capturing the transition between crack shapes that do not conform to the underlying mesh. The effect of the range of tentative crack directions, defined by $|\Omega_{max}|$, was assessed. The results obtained indicate that enabling the algorithm to search for a maximum ERR, by varying the tentative crack direction, is key to obtaining a framework that does not result in the development of non-physical crack shapes. The sensitivity study performed in Section 4.3.1 suggests that mesh size, release tolerance and crack increment affect the smoothness of the results. Decreasing either of these tolerances or the mesh size leads to progressively smoother solutions at the expense of longer computational times. As proposed, the progressive release scheme only requires the solution of a linear system of equations and hence does

not show convergence difficulty.

6. Concluding Remarks

An approach is proposed that combines progressive nodal release with the VCCT to model fatigue crack growth in a mesh-independent fashion. Three new aspects are worth highlighting:

1. VCCT expressions are proposed that generalize the calculation of ERR for nodes at the crack front that have not yet started to release and for nodes that are partially released.
2. ERRs along the crack front are calculated via a new procedure that explicitly accounts for the local shape of the crack front and does not assume a local crack growth direction aligned with mesh lines
3. Aspects 1 and 2 were combined with a progressive release scheme that is formulated such that no artificial crack growth or healing occurs as a result of a change in loading conditions.

The approach was implemented as a user element in Abaqus/Standard® and assessed by comparing results obtained from simulating DCB, MMB and ENF test specimens with existing 2D benchmarks. This comparison enabled the assessment of the approach for mode-mixity ranging from Mode I to Mode II. Overall, the results compared well to the 2D benchmarks, demonstrating the accuracy of the approach for the cases tested. The approach was further assessed by applying it to the simulation of growth of circular and elliptical embedded cracks. These simulations qualitatively demonstrated the ability of the approach to capture the transition between crack shapes that do not conform to the underlying regular mesh.

The methodology can be used with any functional form of ERR that characterizes delamination growth rate under mixed-mode conditions. It does not require any dedicated material model calibration or characterization. Crack growth is determined as a post-processing step at the end of each increment, and hence it shows no convergence issues associated with the progressive nodal release. Overall, the results obtained suggest the approach may provide a suitable strategy to simulate mixed-mode fatigue delamination growth in composite laminates.

Acknowledgements

The material is based upon work supported by NASA under Award No. NNL09AA00A. Any opinions, findings, and conclusions or recommendations expressed in this material are those of the author(s) and do not necessarily reflect the views of the National Aeronautics and Space Administration.

References

[1] T.E. Tay. Characterization and analysis of delamination fracture in composites: An overview of developments from 1990 to 2001. *Applied Mechanics Reviews*, 56(1):1–32, 2003.

[2] E.F. Rybicki and M.F. Kanninen. A finite element calculation of stress intensity factors by a modified crack closure integral. *Engineering Fracture Mechanics*, 9(4):931 – 938, 1977.

[3] R. Krueger. Virtual crack closure technique: history, approach, and applications. *Applied Mechanics Reviews*, 57(2):109 – 143, 2004.

[4] M.F.S.F. De Moura, J.P.M. Gonçalves, A.T. Marques, and P.M.S. Tavares De Castro. Modeling compression failure after low velocity impact on laminated composites using interface elements. *Journal of Composite Materials*, 31(15):1462 – 1479, 1997.

[5] P.P. Camanho and C.G. Dávila. Mixed-mode decohesion finite elements for the simulation of delamination in composite materials. Technical report, NASA-TM-2002-211737, National Aeronautics and Space Administration, 2002.

[6] M. Latifi, F.P. van der Meer, and L.J. Sluys. A level set model for simulating fatigue-driven delamination in composites. *International Journal of Fatigue*, 80:434 – 442, 2015.

[7] Y. Hu and E. Madenci. Peridynamic modeling of fatigue damage in notched composite laminates. In 58^{th} *AIAA/ASCE/AHS/ASC Structures, Structural Dynamics, and Materials Conference*, AIAA SciTech Forum. American Institute of Aeronautics and Astronautics, January 2017.

[8] R. Krueger and N.V. De Carvalho. In search of a time efficient approach to crack and delamination growth predictions in composites. In *Proceedings of the American Society for Composites* 31^{st} *Technical Conference*, number 2606, Williamsburg, VA, USA, 2016.

[9] K. Kiefer. *Simulation of High-Cycle Fatigue-Driven Delamination in Composites Using a Cohesive Zone Model*. PhD thesis, Imperial College London, 2014.

[10] B.L.V. Bak, A. Turon, E. Lindgaard, and E. Lund. A benchmark study of simulation methods for high-cycle fatigue-driven delamination based on cohesive zone models. *Composite Structures*, 164:198 – 206, 2017.

[11] S. Rinderknecht and B. Kröplin. A computational method for the analysis of delamination growth in composite plates. *Computers & Structures*, 64(1):359 – 374, 1997.

[12] P. Robinson, T. Besant, and D. Hitchings. Delamination growth prediction using a finite element approach. In J.G. Williams and A. Pavan, editors, *Fracture of Polymers, Composites and Adhesives*, volume 27 of *European Structural Integrity Society*, pages 135 – 147. Elsevier, 2000.

[13] B.R. Davis, P.A. Wawrzynek, and A.R. Ingraffea. 3-D simulation of arbitrary crack growth using an energy-based formulation - part I: Planar growth. *Engineering Fracture Mechanics*, 115:204 – 220, 2014.

[14] L. Deobald, G. Mabson, B. Dopker, and D. Graesser. Interlaminar fatigue elements for crack growth based on virtual crack closure technique. In 48^{th} *AIAA/ASME/ASCE/AHS/ASC Structures, Structural Dynamics and Materials Conference*, 2007.

[15] N.V. De Carvalho and R. Krueger. Modeling fatigue damage progression and onset in composites using an element-based virtual crack closure technique combined with the floating node method. In *Proceedings of the American Society for Composites* 31^{st} *Technical Conference, Williamsburg, VA, USA, 2016*, number 1102, 2016.

[16] De Xie and S.B. Biggers Jr. Strain energy release rate calculation for a moving delamination front of arbitrary shape based on the virtual crack closure technique. part I: Formulation and validation. *Engineering Fracture Mechanics*, 73(6):771 – 785, 2006.

[17] A. C. Orifici, R. S. Thomson, R. Degenhardt, C. Bisagni, and J. Bayandor. Development of a finite-element analysis methodology for the propagation of delaminations in composite structures. *Mechanics of Composite Materials*, 43(1):9–28, 2007.

[18] E. Pietropaoli and A. Riccio. On the robustness of finite element procedures based on virtual crack closure technique and fail release approach for delamination growth phenomena. Definition and assessment of a novel methodology. *Composites Science and Technology*, 70(8):1288 – 1300, 2010. ISSN 0266-3538.

[19] G.E. Mabson, L.R. Deobald, B. Dopker, D.M. Hoyt, J.S. Baylor, and D.L. Graesser. Fracture interface elements for static and fatigue analysis. In 16^{th} *International Conference on Composite Materials*, 2007.

[20] *Abaqus Analysis User's Manual, Abaqus/Standard®*. DSS Simulia, 6.17 edition, 2017.

[21] N.V. De Carvalho, R. Krueger, G.E. Mabson, and L.R. Deobald. Combining progressive nodal release with

the virtual crack closure technique to model fatigue delamination growth without re-meshing. In *2018 AIAA/ASCE/AHS/ASC Structures, Structural Dynamics, and Materials Conference*. American Institute of Aeronautics and Astronautics, January 2018.

[22] B.Y. Chen, S.T. Pinho, N.V. De Carvalho, P.M. Baiz, and T.E. Tay. A floating node method for the modelling of discontinuities in composites. *Engineering Fracture Mechanics*, 127:104 – 134, 2014.

[23] C. Rans, R. Alderliesten, and R. Benedictus. Misinterpreting the results: How similitude can improve our understanding of fatigue delamination growth. *Composites Science and Technology*, 71(2):230 – 238, 2011.

[24] G. Allegri, M.R. Wisnom, and S.R. Hallett. A new semi-empirical law for variable stress-ratio and mixed-mode fatigue delamination growth. *Composites Part A: Applied Science and Manufacturing*, 48: 192 – 200, 2013.

[25] R. Krueger. Development of a benchmark example for delamination fatigue growth prediction. Technical Report NASA/CR-2010-216723, National Aeronautics and Space Administration, 2010.

[26] R. Krueger. Development and application of benchmark examples for mode II static delamination propagation and fatigue growth predictions. Technical Report NASA/CR-2011-217305, National Aeronautics and Space Administration, 2011.

[27] B.D. Davidson. An analytical investigation of delamination front curvature in double cantilever beam specimens. *Journal of Composite Materials*, 24(11):1124–1137, 1990.